Acta Materialia 274 (2024) 119995

Contents lists available at ScienceDirect

Acta Materialia

journal homepage: www.elsevier.com/locate/actamat

Full length article

First-principles thermodynamics of precipitation in aluminum-containing refractory alloys

Yann L. Müller [a], Anirudh Raju Natarajan [a,b,*]

[a] Laboratory of Materials Design and Simulation (MADES), Institute of Materials, École Polytechnique Fédérale de Lausanne, Switzerland
[b] National Centre for Computational Design and Discovery of Novel Materials (MARVEL), École Polytechnique Fédérale de Lausanne, Switzerland

ARTICLE INFO

Dataset link: https://doi.org/10.24435/materialscloud:th-d5

Keywords:
Cluster expansion
Alloy theory
Density functional theory (DFT)
Precipitation
Phase stability
Thermodynamics

ABSTRACT

Materials for high-temperature environments are actively being investigated for deployment in aerospace and nuclear applications. This study uses computational approaches to unravel the crystallography and thermodynamics of a promising class of refractory alloys containing aluminum. Accurate first-principles calculations, cluster expansion models, and statistical mechanics techniques are employed to rigorously analyze precipitation in a prototypical senary Al–Nb–Ta–Ti–V–Zr alloy. Finite-temperature calculations reveal a strong tendency for aluminum to segregate to a single sublattice at elevated temperatures. Precipitate and matrix compositions computed with our *ab-initio* model are in excellent agreement with previous experimental measurements (Soni et al., 2020). Surprisingly, conventional B2-like orderings are found to be both thermodynamically and mechanically unstable in this alloy system. Complex anti-site defects are essential to forming a stable ordered precipitate. Our calculations reveal that the instability of B2 compounds can be related to a simple electron counting rule across all binary alloys formed by elements in groups 4,5, and 6. The results of this study provide viable routes toward designing high-temperature materials for deployment in extreme environments.

Structural alloys that can withstand temperatures exceeding 1000 °C are urgently needed to replace conventional materials used in aerospace and nuclear applications [1–6]. Multi-component refractory alloys comprising elements in groups 4, 5, and 6 of the periodic table are attractive candidates due to their high melting points and tunable mechanical properties [6–11]. However, single-phase disordered multicomponent refractory alloys may not have sufficiently high mechanical strength for high-temperature structural applications [1,12–14].

Precipitation hardening is a promising route that could improve the strength of refractory alloys. Age hardening is commonly used to tune material properties in aerospace, automotive, and energy applications [15–18]. For example, binary nickel–aluminum alloys form a thermally stable microstructure comprised of ordered γ' precipitates embedded within a disordered γ phase. The $\gamma - \gamma'$ microstructure, together with the careful choice of alloying elements has led to the successful deployment of modern nickel-based superalloys with superior high-temperature strength and creep resistance in gas turbine engines [19–22].

Forming a fine distribution of second-phase particles in refractory alloys is challenging. Mixing elements from groups 4,5 and 6 results in the formation of either disordered solid solutions or complex intermetallics such as the Laves phase [23,24]. The coarse precipitate sizes and the inherent brittleness of Laves phases typically degrade the mechanical strength of refractory alloys. A significant strength increment requires the formation of a nanoscale distribution of coherent ordered precipitates. Precipitate phases capable of forming such microstructures are thermodynamically unstable in alloys containing only refractory elements [23,25–28].

The addition of aluminum to transition metal alloys can induce precipitate formation [1,3,29,30]. Early studies by Naka and Khan [1] on aluminum-containing refractory alloys, reported the synthesis of a single-phase microstructure comprised of an ordering on the body-centered cubic crystal structure. Subsequent studies demonstrated that a two-phase microstructure with a disordered bcc solid solution embedded within a continuous ordered bcc phase could be achieved through modifications to alloy chemistry [12,31–42]. However, samples synthesized in these earlier studies were not ductile due to the inherent brittleness of the ordered intermetallic matrix phase. Elements such as ruthenium have recently been shown to also promote the formation of second-phase intermetallic precipitates [43].

Two-phase microstructures with a continuous disordered solid solution have only been recently synthesized. A study by Soni et al. [39] reported the synthesis of an ordered precipitate within a disordered bcc

* Corresponding author at: Laboratory of Materials Design and Simulation (MADES), Institute of Materials, École Polytechnique Fédérale de Lausanne, Switzerland.
E-mail address: anirudh.natarajan@epfl.ch (A.R. Natarajan).

https://doi.org/10.1016/j.actamat.2024.119995
Received 6 February 2024; Received in revised form 3 May 2024; Accepted 9 May 2024
Available online 11 May 2024

matrix in the 6-component Al–Nb–Ta–Ti–V–Zr system. Starting from a disordered microstructure, the authors aged the 6-component alloy at 600 °C. During the initial stages of ageing, the microstructure shows a dense continuous network of an ordered phase with the disordered phase appearing as cuboidal inclusions. Upon further ageing, the disordered inclusions coarsen and develop necking constrictions along channels of the ordered phase. Eventually, a continuous disordered phase emerges due to a narrowing of these constrictions. Interestingly, the ordered precipitates formed in this alloy system are found to show similar diffraction patterns to that of the well-known B2 ordering. Further analysis of atom probe data revealed that the ordered phase is essentially a ternary precipitate containing Al, Ti, and Zr.

Despite several decades of research into refractory alloys containing aluminum, the precise crystal structure of the intermetallic bcc ordering obtained in previous studies remains elusive. The ordered phase is referred to as "B2" in the literature as superlattice Bragg peaks similar to that of the conventional B2 ordering are observed. The B2 ordering is typically formed in binary alloys, with one element located on the corners of the conventional bcc cell, while the other element is located at the body-center. The formation of multi-component B2 precipitates necessitates either the dissolution of various elements on the two sublattices of B2 in a random manner or the formation of a more complex B2 ordering such as the Heusler-type structures. However, the exact sublattice occupancies and ordering in aluminum-containing refractory alloys remain open questions. In fact, the formation of B2-like precipitates in multicomponent refractory alloys with aluminum is quite surprising as B2 orderings are typically not observed in any of the binary phase diagrams. *Ab-initio* crystal structure databases such as OQMD [44,45], MaterialsProject [46], AFLOW [47], etc. estimate that B2 orderings formed by aluminum and a refractory element are unstable by $\approx$ 0.1–0.4 eV/atom.

In this study, we use first-principles calculations together with statistical mechanics techniques to unravel the crystal structure and thermodynamic stability of ordered phases on the bcc crystal structure in aluminum-containing refractory alloys. We begin by rigorously analyzing the metastable and stable thermodynamics of the senary Al–Nb–Ta–Ti–V–Zr alloy. Accurate cluster expansion models are used with Monte-Carlo simulations to reveal the strong segregation of aluminum to a single sublattice of the B2 structure at elevated temperatures. Precipitate and matrix composition calculated with our atomistic model are in excellent agreement with the experimental observations of Soni et al. [39]. Taken together, our results indicate that the precipitate phase formed in experiment has long-range order similar to the B2 phase due to the strong segregation of aluminum to a single sublattice. The formation of B2-like long-range order is found to arise from low-temperature orderings within a narrow composition range where aluminum strongly segregates to one sublattice. Our calculations show that the binary B2 structure is both thermodynamically and mechanically unstable at low temperatures suggesting that the formation of ordered precipitate phases may be limited to a narrow range of aluminum compositions. Electronic structure calculations reveal that the instability of binary B2 compounds is due to an insufficient number of valence electrons in aluminum-containing refractory alloys. Finally, careful analysis of structural phase transitions suggests potential transformation pathways for the ordered precipitate to transform into more stable complex intermetallic phases.

1. Methods

Density functional theory (DFT) calculations and statistical mechanics methods are used to predict finite-temperature phase stability in the senary Al–Nb–Ta–Ti–V–Zr alloy. A disordered solid solution and a ternary ordered precipitate on the bcc structure are formed during the age hardening of this alloy [39,48]. Cluster expansion Hamiltonians are ideal tools to study such order–disorder phase transformations at elevated temperatures [49,50].

Within cluster expansion models, orderings of c chemical elements on a *parent* bcc crystal structure are described by assigning occupation variables, σ_i to each site i. The occupation variable (σ_i) represents the chemical specie that occupies site i. Any arrangement of elements on the bcc lattice can then be represented as a vector of site occupation variables $\vec{\sigma} = \{\sigma_1, \sigma_2, \ldots, \sigma_N\}$. The formation energy ($E_f(\vec{\sigma})$) of an arbitrary ordering is expanded as a function of cluster basis functions [49,50]:

$$E_f(\vec{\sigma}) = V_0 + \sum_{\alpha} V_\alpha \Phi_\alpha(\vec{\sigma}) \tag{1}$$

where V_i are constant expansion coefficients that are also known as effective cluster interactions (ECI), and $\Phi_\alpha(\vec{\sigma})$ are cluster basis functions that are polynomials of the site basis functions (ϕ_m):

$$\Phi_\alpha(\vec{\sigma}) = \prod_{(i,m)\in\alpha} \phi_m(\sigma_i) \tag{2}$$

Site basis functions derived from Chebyshev polynomials are used through out this study. Though the expansion of Eq. (1) is a sum over all possible clusters of sites α, in practice, the sum must be truncated at some maximal cluster size. The unknown ECI of a truncated cluster expansion can be estimated by training Eq. (1) to reproduce the formation energies computed with DFT.

Formation energies of symmetrically distinct orderings are parameterized with the cluster expansion formalism as implemented in the *Clusters Approach to Statistical Mechanics (CASM)* software package [51–54]. Total energies are calculated with the generalized gradient approximation (GGA-PBE) to density functional theory (DFT) and projector augmented-wave (PAW) pseudopotentials as implemented in the *Vienna Ab-Initio Simulation Package (VASP)* [55,56]. The pseudopotentials for Al, Nb, Ta, Ti, V, and Zr contained 3, 13, 11, 12, 13, and 12 valence electrons each. A plane-wave cutoff energy of 550 eV with a k-point grid density of 55 Å and a smearing of 0.1 eV were used to relax the positions of atoms and lattice parameters of all orderings.

Two different cluster expansion models were parameterized for this study. The ordered precipitate is predominantly composed of Al, Ti, and Zr [38,39]. A ternary cluster expansion, trained to reproduce the zero Kelvin energies of 576 decorations of titanium, aluminum, and zirconium on bcc, was used to model the effect of ordering in the precipitate phase. ECI were estimated with the LASSO method [57]. The regularization for the LASSO model was chosen by minimizing a 10-fold cross-validation score with the `sklearn`[58] package. Care was taken to reproduce the essential metastable bcc ground states within the ternary Al–Ti–Zr system by introducing weights that are related to the energies of each configuration relative to the energies of the ground states [53]. A second cluster expansion was trained to reproduce the disordered state of the 6-component alloy. Formation energies of 254 orderings, including special-quasirandom structures [59] are included within the training dataset to train the senary cluster expansion.

Finite-temperature thermodynamics in the ternary alloy was estimated with canonical Monte-Carlo simulations in a 10 × 10 × 10 supercell of the conventional bcc cell. Cells with compositions spanning the ternary Al–Ti–Zr alloy were cooled from a high temperature to a low temperature. Simulation cells are cooled down from 20'000K to 0 K, first using 500 logarithmic temperature increments down to 5'000K followed by temperature decrements of 5 K. Ensemble averages are collected at each temperature and composition ensuring that ensemble averaged energies are converged to within a precision of 1 meV/atom. Gibbs free energies were then computed as [60]:

$$G(T,\vec{x}) = \frac{T}{T_0} G(T_0,\vec{x}) + T\int_{T_0}^{T} -\frac{\langle E\rangle}{\tau^2} d\tau \tag{3}$$

where $\vec{x}$ is the composition of the cell, T is the temperature, $G(T_0,\vec{x})$ is the reference free energy at T_0, $\langle E\rangle$ is the ensemble average of the energy at a temperature τ and the integral is computed from T_0 to T. The high-temperature disordered free energy at 20,000 K was

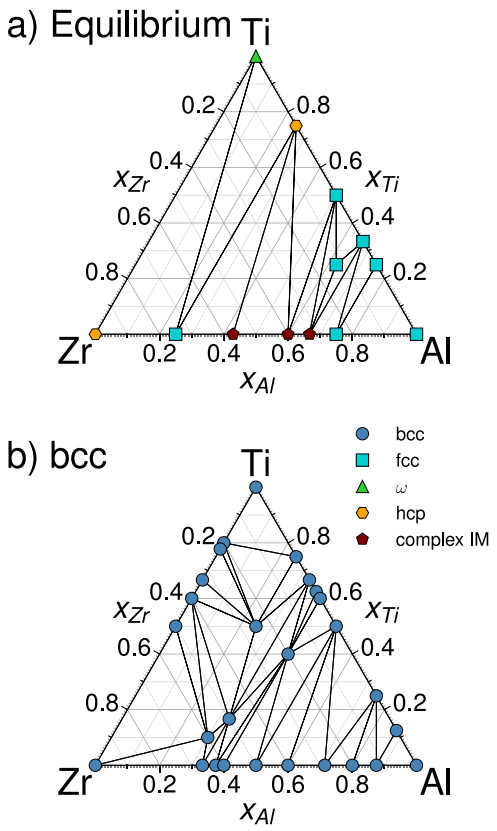

Fig. 1. 0 K phase diagram in the ternary Al–Ti–Zr alloy. (a) Equilibrium phase diagram (b) Metastable phase diagram over orderings on bcc.

approximated using ideal solution entropy and the disordered enthalpy was computed with Monte-Carlo simulations.

A simpler free energy model is adopted for the 6-component disordered solid solution. The enthalpy is approximated by the disordered enthalpy predicted with the cluster expansion, while the entropy is given by ideal solution entropy. Comparison of the solid solution enthalpy between the simple 6-component model and the ternary model at a few different compositions along the binary alloys, i.e., Al–Ti, Al–Zr, and Ti–Zr, showed that the approximate enthalpy errors are less than 16meV/atom.

Long-range order parameters were used to estimate the degree of B2-like order at elevated temperatures. The B2 ordering contains two distinct sublattices. Sublattice compositions of Al, Ti, and Zr computed at each step of the Monte-Carlo simulation are related to long-range order parameters as [61]:

$$\langle \eta_i \rangle = \langle \frac{|x_1^i - x_2^i|}{2} \rangle \tag{4}$$

where x_j^i is the sublattice composition of element i on sublattice j, η_i is the long-range order parameter tracking the degree of B2-like order for specie i and $\langle . \rangle$ denotes ensemble averages. Ensemble averages of long-range order parameters were rescaled with the global alloy composition so that they always lie between zero (representing the disordered phase) and one. A long-range order parameter value of one indicates that the cell has the maximal degree of B2-like order that is achievable at a given alloy composition. A value of 1 for the long-range order parameter, η_i, can equivalently be interpreted as complete segregation of specie i to a single sublattice.

2. Results

We begin by analyzing zero Kelvin phase stability in the ternary Ti–Al–Zr alloy. The 0 K equilibrium phase diagram of Fig. 1a is computed based on the formation energies of all crystal structures found on the Open Quantum Materials Database (OQMD) [44,45] and symmetrically distinct arrangements of the three elements on the bcc crystal structure. The formation energy of a configuration ($\vec{\sigma}$) relative to ω-titanium, hcp-zirconium and fcc aluminum is given by:

$$E_f(\vec{\sigma}) = \frac{1}{N}(E(\vec{\sigma}) - N_{Al}E_{Al}^{fcc} - N_{Ti}E_{Ti}^{\omega} - N_{Zr}E_{Zr}^{hcp}) \tag{5}$$

where $E_f(\vec{\sigma})$ is the formation energy per atom, N is the number of atoms in the unit cell, $E(\vec{\sigma})$ is the total energy calculated with DFT, N_{Al}, N_{Ti}, N_{Zr} are the number of aluminum, titanium, and zirconium atoms and E_{Al}^{fcc}, E_{Ti}^{ω}, E_{Zr}^{hcp} are the total energies of Al, Ti, and Zr in the fcc, ω, and hcp crystal structures. Thermodynamic stability at zero Kelvin is estimated by constructing the convex hull over the formation energies of all configurations.

The equilibrium phase diagram for the ternary alloy at 0 K is shown in Fig. 1a. Orderings on the face-centered cubic crystal structure are predicted to be stable at aluminum-rich compositions. Titanium and zirconium-rich compositions are predicted to form orderings with an underlying hcp and ω crystal structure. Intermetallic compounds with complex crystal structures such as hP7-Al_3Zr_4, C14-Al_2Zr, oF40-Al_3Zr_2 are found to be stable along the Al–Zr binary. Phases predicted to be stable at 0 K are in close agreement with experimental studies in the ternary alloy [62–64]. High-temperature phases such as B33-AlZr, $D8_8$-Al_4Zr_5, tP20-Al_2Zr_3, D8m-Al_3Zr_5, and $B8_2$-$AlZr_2$ are not predicted to be stable at 0 K. These compounds may be stabilized at elevated temperatures due to entropic contributions. Though ordered precipitates with a bcc crystal structure are observed in experiment [39], no such orderings are predicted to be on the equilibrium phase diagram at 0 K.

Orderings on the same crystal structure as the disordered solid solution are often formed during the early stages of precipitation hardening due to small nucleation barriers [16,17]. The metastable phase diagram constructed over orderings on bcc can shed light on the crystal structures of ordered precipitates formed in the initial stages of ageing. The 0 K metastable phase diagram across orderings on the bcc crystal structure is shown in Fig. 1b. Structures are classified as bcc based on a similarity metric [65] computed between the fully relaxed structure and bcc. First, a structure score is computed to estimate the similarity between the relaxed ordering and 4 parent crystal structures (bcc, hcp, fcc, and ω). The ordering is assigned to the parent structure with the highest similarity (i.e., lowest score). Orderings with a score smaller than 0.014 are used to compute the metastable convex hull for bcc.

The metastable phase diagram of Fig. 1b predicts the formation of several ordered ground states at 0 K. Orderings are predicted to be stable not just along the three binaries but also at ternary compositions. Metastable bcc orderings are predicted to be $\approx$ 50 meV/atom above the convex hull at aluminum compositions around $x_{Al} \approx 0.4$. While these orderings are unlikely to be stabilized through vibrational entropy at elevated temperatures, they could be formed as transient metastable structures during the heat treatment of disordered bcc solid solutions.

Interestingly, ground states on the metastable bcc convex hull with stoichiometries close to equiatomic aluminum–zirconium compositions have very simple crystal structures. Fig. 2 depicts the crystal structures of ground state orderings on bcc. All ground states in Fig. 2 can be viewed as two-dimensional arrangements of Al, Ti, and Zr rods extending along the [001] direction. For instance, Fig. 2a shows the crystal structure of the zirconium-rich, Al_4Zr_8 groundstate. Two adjacent (001) planes are drawn in the two-dimensional projection of Fig. 2a - atoms on one of the (001) planes correspond to the atoms at the corners of the square lattice, while atoms in the neighboring layer (either above or below) are located at the centers of the squares. The (001) layers drawn on the corners and centers of the squares are located at different heights along the [001] direction. The Al_4Zr_8 ground state is made of zirconium rods (shown in green) that fill an entire (001) plane. The adjacent (001) planes contain both aluminum and zirconium rods.

The two (001) planes located at the corners and centers of the square lattice also correspond to the two sublattices found in a binary

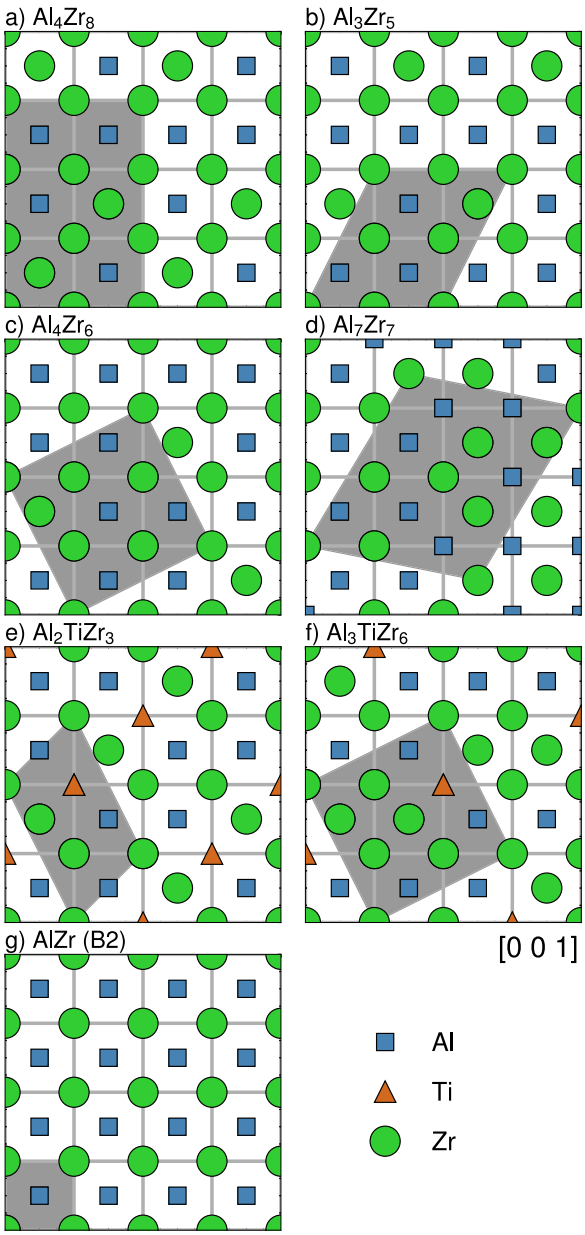

Fig. 2. Schematic drawings of: (a) to (f) some Al–Zr-rich ground state orderings in bcc, and (g) B2 ordering, viewed along the [001] direction. Blue squares, orange triangles, and green circles represent rods of Al, Ti, and Zr, respectively, extending along the [001] direction.

B2 ordering. The B2 ordering (Fig. 2g) when viewed along the [001] direction, contains two chemical elements located at either the corners or centers of the square lattice. The Al_4Zr_8 ground state has long-range order similar to B2 as all aluminum atoms occur on a single sub-lattice located at the centers of the squares. The "excess" zirconium atoms are accommodated as "defects" on the aluminum sublattice. Ground-states that are rich in the refractory elements display a similar trend in Fig. 2. As the aluminum concentration increases from Al_4Zr_8 to Al_4Zr_6, some of the zirconium atoms on the aluminum sublattice are replaced with Al. The precise ordering of aluminum and zirconium differs slightly across stoichiometries. Al_4Zr_8 and Al_3Zr_5 contain alternating rods of aluminum and zirconium atoms on a single (010) plane. Both ground states contain a single layer of pure aluminum that separates two (010) planes that contain both aluminum and zirconium rods.

The segregation of aluminum to a single sublattice persists upon small additions of titanium. The ground states of Fig. 2e and f suggest that titanium segregates to the zirconium-rich sublattice at low temperatures. Intriguingly, titanium is also found to occur as rods extending along the [001] direction.

Ground states with aluminum compositions near $x_{Al} \approx 0.5$ do not show a strong tendency for aluminum to segregate to a single sublattice. The metastable ordering with a stoichiometry of Al_7Zr_7 in Fig. 2d contains aluminum and zirconium rods across both sublattices of the ideal B2 ordering. The equiatomic ordering that is predicted to be stable at 0 K is thus different from an ideal B2 phase and does not have long-range B2 order.

High-temperature phase stability was estimated by minimizing free energies computed from Monte-Carlo simulations based on a cluster expansion Hamiltonian. The ternary cluster expansion parameterized over orderings of Al, Ti, and Zr had a root mean square error of 9 meV/atom and a 10-fold cross-validation score of 15 meV/atom. The cluster expansion reproduced all relevant ground states along the Al–Zr binary and the ground states with dilute additions of titanium. Ground states with high compositions of Al, Ti, or Zr were not reproduced. Ground states predicted by the cluster expansion that are not ground states along the DFT convex hull are found to be within 5 meV/atom of the convex hull. However, as all ground states for experimentally relevant compositions are well-reproduced, this model is sufficiently accurate to model precipitation. The senary cluster expansion had a root mean square error of 9.9 meV/atom.

Ensemble averages of the long-range order parameter (Eq. (4)) and internal energy computed from Monte-Carlo simulations in a cell with a composition of 33.8%, 11.1%, and 55.1% Al, Ti, and Zr are shown in Fig. 3. A first-order phase transition is predicted to occur at a temperature of ≈800 K. The nature of the high- and low-temperature phases are quantified with the long-range order parameters of Eq. (4) in Fig. 3b. Three long-range order parameters are computed with the sublattice compositions of aluminum, titanium, and zirconium. Long-range order similar to B2 corresponds to an order parameter value of one, while the disordered phase has an order parameter value of zero. At temperatures below 800 K the titanium and aluminum order parameters are close to one. Similar to the ground states of Fig. 2, aluminum and titanium are found to strongly segregate to a single sublattice in the Monte-Carlo simulations. Zirconium occurs on both sublattices at lower temperatures, resulting in an order parameter that is between zero and one. Above the phase transition at 800 K, the titanium order parameter decreases to ≈ 0.2, indicating that titanium is found across both sublattices of the B2 structure at elevated temperatures. Aluminum continues to segregate to a single sublattice even at temperatures exceeding 800 K. The disordered phase is predicted to form at temperatures exceeding ≈ 3600 K in the ternary alloy through a second-order phase transition. All long-range order parameters are close to zero at such high temperatures. Our simulations suggest that a ternary alloy constrained to form the bcc structure is likely to melt before it disorders into a solid solution.

Additional insights into the order–disorder transitions of this system can be derived by investigating Monte-Carlo snapshots at two temperatures. Fig. 3c depicts the ordered phase at two temperatures, 500 and 1500 K. At 500 K, the system contains rods of aluminum, titanium, and zirconium extending along ⟨001⟩. Most rods are made of only a single element with occasional point defects arising due to entropic effects. Aluminum segregates to one sublattice of B2 while titanium segregates to the other sublattice at low temperatures. The system partially disorders at temperatures exceeding 800 K. Rods of Al, Ti, and Zr are found to contain a larger number of defects than the low-temperature phase. Additionally, we also predict that titanium atoms are distributed over both sublattices of B2, i.e. on both the aluminum and zirconium-rich sublattices. The elevated concentration of titanium on the aluminum sublattice lowers the long-range order parameter of Ti below one. Our Monte-Carlo simulations are in agreement with experiment as we predict the existence of a partially ordered phase containing B2-like order due to the segregation of aluminum.

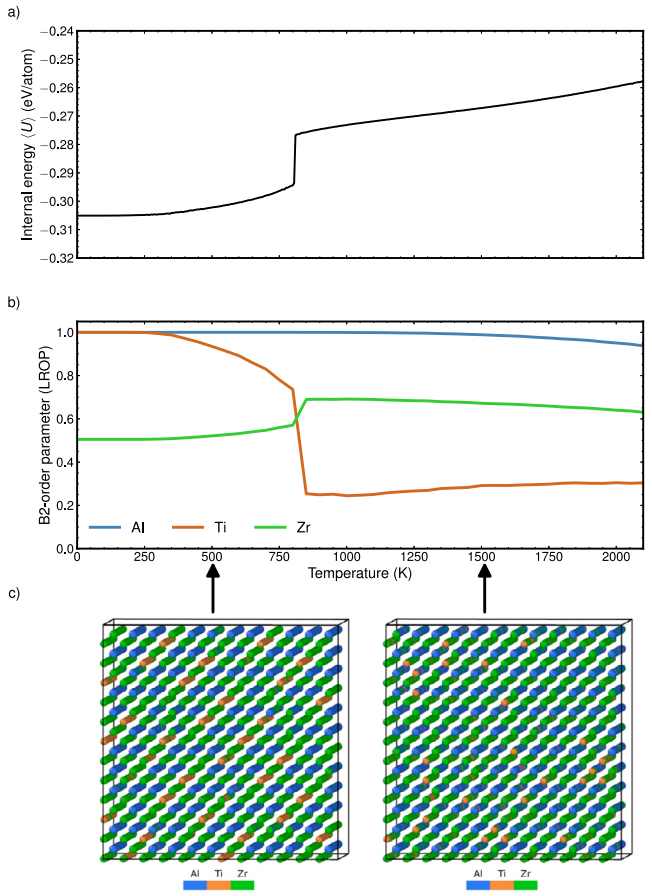

Fig. 3. Plots of (a) the internal energy and (b) the long-range order parameter (LROP) normalized by the concentration as a function of the temperature. Snapshots of the simulation cell at 500 K and 1500 K are shown in (c). All data are obtained from canonical Monte Carlo simulations with a composition of 33.8 at.%Al 11.1 at.%Ti 55.1 at.%Zr.

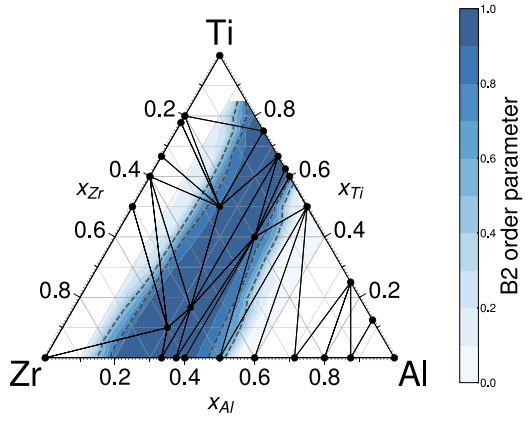

Fig. 4. Ternary plot with the computed long-range B2 order parameters evaluated at 1375 K for aluminum. Strong segregation of aluminum at compositions between 0.2 and 0.4 is predicted. The metastable bcc convex hull is also shown in the figure.

Aluminum is predicted to segregate to a single sublattice across a narrow band of ternary compositions. Our finite-temperature simulations at 1000 °C, shown in Fig. 4, suggests the persistence of B2-like order for aluminum compositions between $\approx 0.2 - 0.4$. Interestingly, the segregation of aluminum, and thus long-range B2-like order vanishes as the aluminum composition approaches $x_{\mathrm{Al}} = 0.5$. Our

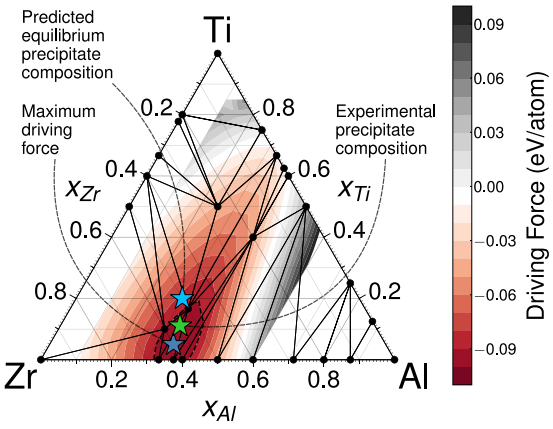

Fig. 5. Plot of the computed thermodynamic driving force to form an ordered precipitate from a supersaturated solid-solution at 600 °C. The composition of the precipitates observed experimentally in Ref. [39] is indicated by a green star. The composition with the highest driving force and the equilibrium composition are shown as blue stars.

Table 1
Comparison between the predicted and experimentally measured [39] compositions of the phases observed after aging a senary alloy at 600 °C for 120 h.

		Al	Nb	Ta	Ti	V	Zr	Phase fraction
Precipitate	Exp.	32.4	2.2	0.2	10.6	0.2	52.8	30.2
	Comp.	30	0	0	20	0	50	33
Matrix	Exp.	1.8	24.1	17.3	33.5	6.9	7.4	69.8
	Comp.	0	30	24	35	6	5	67

high-temperature simulations are in agreement with the lack of low-temperature ground states with long-range B2-like order at equiatomic aluminum compositions.

Finite-temperature phase stability and driving forces for precipitation were estimated from the free energies of the ternary precipitate phase and the disordered senary solid solution. Equilibrium phase stability is estimated by constructing the common tangent between the Gibbs free energies of the ordered and disordered states. The alloy composition reported in the experiment by Soni et al. [38] is used as the total alloy composition. In the early stages of ageing, precipitate compositions with the highest thermodynamic driving force are likely to be formed. At longer ageing times, the precipitate should evolve towards its true equilibrium composition. The equilibrium composition and the composition with the largest driving force provide a range of plausible compositions that may be transiently observed during precipitation.

Fig. 5 and Table 1 show the measurements from experiments together with our predictions from theory for a $Al_{0.5}NbTa_{0.8}Ti_{1.5}V_{0.2}Zr$ alloy aged at 600 °C. Precipitate compositions predicted by theory are in excellent agreement with experimental measurements. In fact, the precipitate composition is found to lie between the composition with the highest thermodynamic driving force and the equilibrium precipitate composition. The predictions of Table 1 also show very good agreement with the experimentally measured volume fraction of the two phases.

3. Discussion

This study has focused on unraveling the crystal structure and thermodynamic stability of ordered precipitates formed in a senary Al–Nb–Ta–Ti–V–Zr alloy. Our calculations show that precipitates formed during the early stages of ageing in the senary alloy are partially ordered phases that emerge from the ternary Al–Ti–Zr system. Aluminum atoms are predicted to segregate to a single sublattice of the

B2 structure while titanium and zirconium are disordered over both sublattices at elevated temperatures. Orderings on the bcc crystal structure are metastable relative to more complex phases as shown in Fig. 1. The ordered phase is likely metastable even at elevated temperatures and should dissolve to form more stable and complex intermetallic compounds at longer ageing times. Monte-Carlo simulations using a cluster expansion parameterized from the DFT formation energies reveal that long-range order due to aluminum segregation persists at elevated temperatures and across a large part of the ternary composition space (Fig. 4). However, the long-range B2-like order vanishes as the aluminum composition approaches 0.5. Precipitate composition and volume fraction predicted with our model are in excellent agreement with the values measured in experiment.

The finite-temperature free energies derived from our cluster expansion serve as a valuable tool to guide alloy designers. For instance, the model can be used to identify compositional modifications to the alloy used in [39] that may form precipitates with higher solvus temperatures. Using the free energies obtained from our rigorous statistical mechanics simulations, we computed the solvus temperatures of precipitates formed in alloys with compositions similar to those studied by Soni et al. [39]. Solvus temperatures of ordered phases were computed by estimating the temperature at which the driving force to form an ordered phase from a disordered phase is zero. Our calculations suggest that the thermal stability of the precipitates may be improved by increasing the concentrations of aluminum and zirconium or vanadium and tantalum, while simultaneously reducing the niobium content. However, increasing the vanadium composition is generally undesirable due to the low melting temperature of its oxide. Increasing the concentration of aluminum and zirconium could induce the formation of more complex intermetallic phases.

It is important to note that there could be quantitative discrepancies between theory and experiment due to several reasons. One possible source of error is the lack of vibrational entropy in our free energy model. Anharmonic vibrations play an important role in stabilizing bcc phases that are rich in titanium and zirconium [66]. These effects are likely to be more pronounced at higher temperatures. Additionally, our thermodynamic model for the ordered precipitate is restricted to the ternary composition space spanned by Al–Ti–Zr. As a result, we are unable to capture the small amounts of vanadium, tantalum, and niobium seen in experiment. Coherency strains, and interfacial free energies could also play a significant role in determining precipitate compositions as the precipitates are formed coherently or semi-coherently within the microstructure. Finally, even small amounts of oxygen contamination could have marked effects in experiment that would not be reproduced by our model [67,68].

3.1. Thermodynamic and mechanical stability of B2

Though B2-like long-range order is observed in experiments, the conventional B2 ordering with an aluminum composition of 0.5 is not stable. Sections of the 0 K formation energy along the three binaries and along a line with $x_{Zr} = 0.5$ are shown in Fig. 6. Phases on the black line are thermodynamically stable at 0 K while the blue line in Fig. 6 corresponds to the metastable convex hull constructed over orderings on bcc. The results of Fig. 6 show that orderings on bcc are thermodynamically competitive near binary equiatomic compositions. Aluminum-rich concentrations tend to destabilize bcc orderings, with complex intermetallic phases being more stable.

Surprisingly, B2 and related orderings such as $D0_3$ and $L2_1$ are not predicted to be thermodynamically stable at 0 K in the ternary Al–Ti–Zr alloy. The formation energies of B2, $D0_3$, and $L2_1$ are indicated by red stars in Fig. 6. $D0_3$, and $L2_1$ show similar long-range order to B2. Al is found on a single sublattice, with additional titanium or zirconium defects being accommodated on the aluminum sublattice in both structure prototypes. The plots of Fig. 6 clearly reveal that B2 and conventional B2-like orderings are not thermodynamically stable at 0 K.

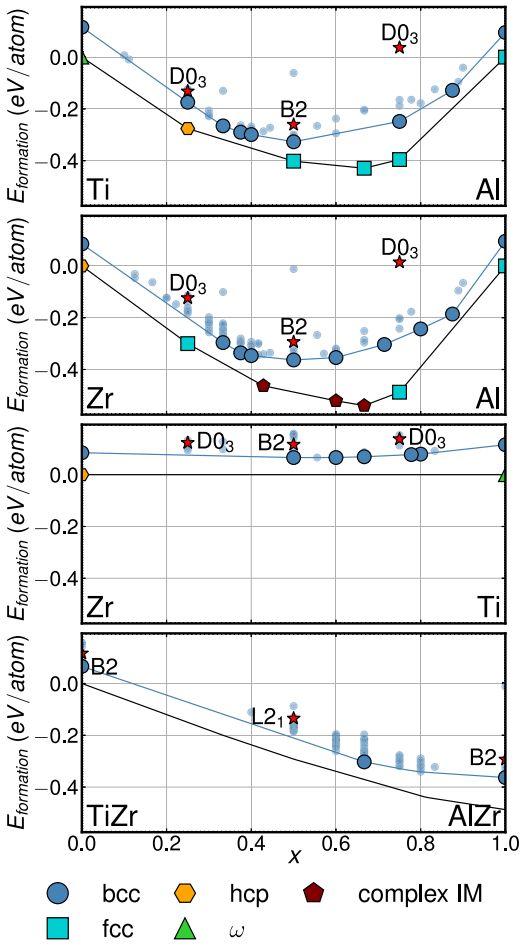

Fig. 6. Plots of binary sections along Ti–Al, Zr–Al, Zr–Ti, and TiZr-AlZr. The formation energies of B2, $D0_3$, and $L2_1$ structures are indicated with red stars. The black and the blue lines correspond to the equilibrium and metastable-bcc convex hulls, respectively, of the ternary Al–Ti–Zr system. (For interpretation of the references to color in this figure legend, the reader is referred to the web version of this article.)

Remarkably, the inclusion of "defects" on the B2 structure stabilizes orderings with long-range B2-like order at aluminum compositions between 0.25 and 0.5. These ground state orderings can be derived by replacing aluminum atoms on the conventional B2 structure with zirconium atoms as shown in Fig. 2.

Binary orderings with the B2 crystal structure are also predicted to be mechanically unstable with respect to structural distortions. First-principles calculations predict binary B2 orderings to be unstable relative to Bain or Burgers distortions, similar to the transformations found in the pure elements of group 4. Straining a body-centered crystal structure along ⟨100⟩ directions can transform the crystal into either fcc (along the Bain path) or hcp (along the Burgers path). The transformation is schematically shown as a function of a strain order parameter (denoted e_3) in Fig. 7. Elongating the reference crystal along [001] results in the formation of fcc, while compressing along this direction transforms the (110) planes of bcc into a triangular lattice. The hcp crystal structure emerges when alternate (110) triangular planes are shuffled. A detailed description of the transformation pathway, order parameters, and shuffle transformations can be found in other studies [23,69].

The energy landscape, computed along the Bain and Burgers path, for B2 AlZr is shown in Fig. 8. DFT calculations predict that the bcc ordering, occurring at $e_3 = 0$, can lower its energy by transforming to either hcp or fcc. The B2 ordering is thus mechanically unstable at 0 K. Interestingly, applying the Burgers shuffle to the ideal B2 ordering is

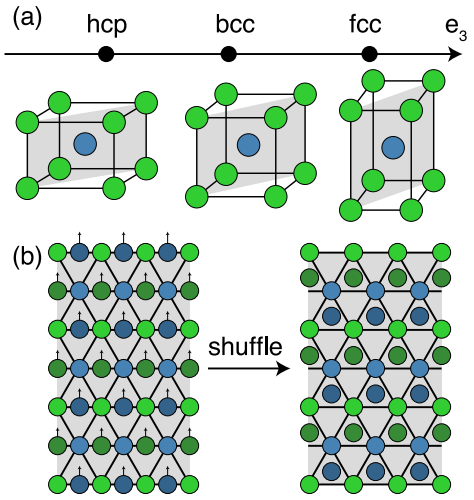

Fig. 7. Schematic drawings of the structural transformations from bcc to fcc and hcp. (a) Structural transformation through strain along e_3. (b) Atomic shuffles of (110) bcc planes needed to form hcp.

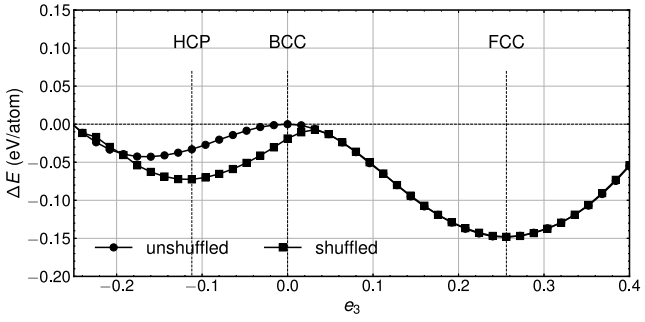

Fig. 8. Strain energy landscape computed with DFT for B2-AlZr along the Bain (unshuffled) and Burgers (shuffled) pathways.

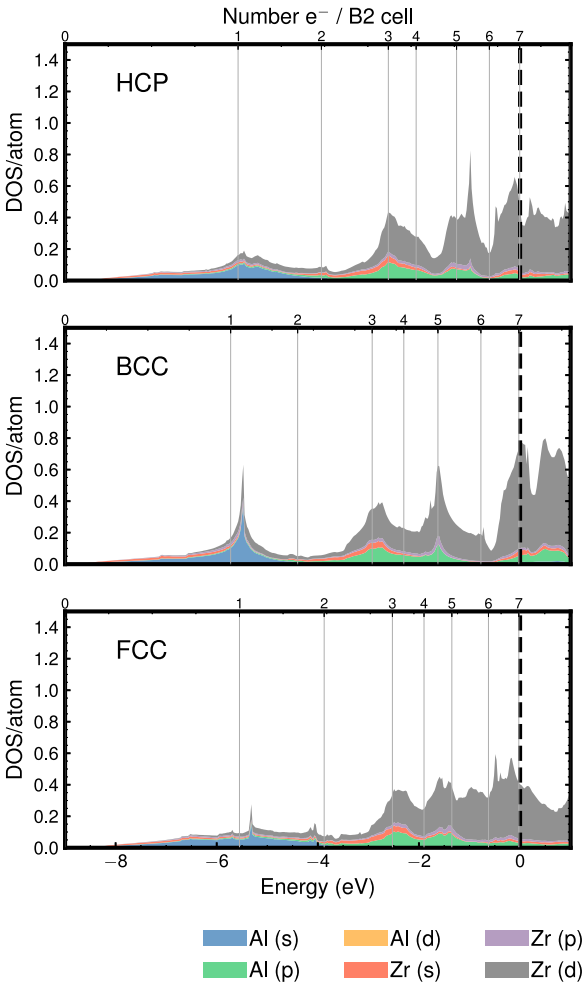

Fig. 9. Plots of the projected density of state for AlZr in structures as follows: hcp (top), bcc B2 (center), fcc $L1_0$ (bottom). The corresponding number of valence electrons per atom is listed at the top of each graph. The Fermi level is indicated by the dashed black line.

predicted to lower the energy of the structure even without the addition of any strain deformations. The instability of this phase is similar to that of pure titanium and zirconium which are also found to be unstable in the bcc crystal structure at 0 K [23].

The structural instability of B2-AlZr can be correlated with an elevated electron density at the Fermi level. The projected density of states for B2-AlZr in Fig. 9 shows several distinctive features. At the Fermi level, there is a sharp peak arising from an elevated density of zirconium *d*-electrons. A small number of aluminum *p* states are also found at the Fermi level, suggesting minimal $p-d$ bonding. The *d*-electron density is significantly lower at energies slightly below and above the Fermi level. Interestingly, *s*-states arising from aluminum are found to be sharply peaked at energies around 6eV below the Fermi level.

Transforming the bcc crystal to either hcp or fcc significantly reduces the density of states at the Fermi-level as depicted in Fig. 9. Zr *d*-states show a shallow valley near the Fermi level in the hcp structure, while the overall electron density is greatly reduced after transformation to the fcc structure. The reduced density at the Fermi level for both hcp and fcc results in a much lower energy as compared with bcc. The structural phase transformation also results in a delocalization of aluminum *s*-states. Charge density plots in the distorted AlZr structure reveal the formation of a delocalized aluminum *s*-state that spans the aluminum sublattice — thus facilitating metallic bonding between aluminum atoms.

First-principles calculations, shown in Fig. 10, predict that nearly every binary B2 ordering comprised of a refractory element with aluminum is mechanically unstable at 0 K. With the exception of aluminum–chromium, all other chemistries are found to be unstable in the bcc crystal structure. The binaries involving group 5 elements are the most unstable, with a transformation from B2 to $L1_0$ in AlTa lowering the energy by almost 300 meV/atom. Projected densities of states computed with DFT in Fig. 11 for each of the unstable binary B2 compounds shows a pronounced peak in the electron density at the Fermi level.

Our analysis of the density of states of binary B2 compounds suggests that the instability and peak in electron density at the Fermi level of B2 are related to the number of valence electrons per atom. It is well-known that valence electron counts around 5 or 6 are required to stabilize the bcc crystal structure in pure elements [70–72]. For instance, titanium contains 4 electrons per atom and is found to occur in the hcp crystal structure. In contrast, elements such as niobium and molybdenum contain 5 and 6 electrons in their valence shell and are found to be stable in the bcc crystal structure. Valence electron counts below 5 typically result in sharply peaked electronic densities near the Fermi level, and induce a Jahn–Teller–Peirls type structural phase transition [73]. The change in structure from bcc to hcp along the Bain transformation opens a pseudogap at the Fermi level in titanium, zirconium, and hafnium.

The simple electron counting rule also predicts the instability of B2 compounds formed by aluminum with the elements of groups 4,

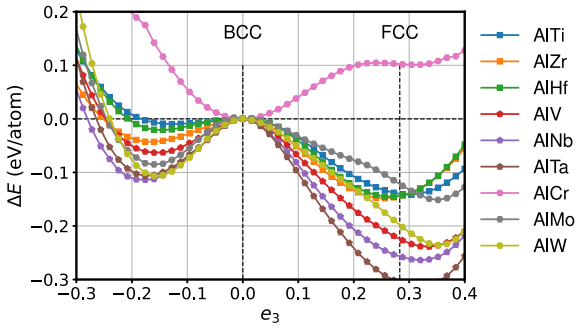

Fig. 10. Energy landscape computed with DFT along the Bain pathway for B2-AlX orderings, with X being an element of group 4, 5, or 6.

5, and 6. Group 4 elements have 4 valence electrons per atom — these include the *d*-electrons and the outer-most *s*-electrons. Aluminum has 3 valence electrons per atom. B2 compounds formed between group 4 elements and aluminum contain 3.5 valence electrons per atom on average. The number of electrons per B2 cell shown in Fig. 9 confirms this. B2 orderings between Al and elements of groups 5 and 6 have 4, and 4.5 valence electrons per atom respectively. Thus all B2 compounds between aluminum and elements of groups 4, 5, and 6 contain less than 5 valence electrons per atom. This correlates with the elevated density around the Fermi level for all binary B2 orderings and the instability of the bcc phase. DFT calculations suggest that the mechanical instability essentially vanishes in B2 compounds formed by aluminum with elements of group 7 (containing 5 valence electrons), as illustrated in Fig. 12 for the B2-AlRe compound.

The instabilities of conventional B2 and B2-like orderings have several consequences. Orderings such as B2, $D0_3$ and $L2_1$ cannot be used to assess the properties of the precipitates observed in aluminum containing refractory alloys. The thermodynamic and finite-temperature analysis based on our cluster expansion model demonstrates the importance of defects. More complex orderings such as those depicted in Fig. 2 together with finite-temperature simulations are required to quantify key inputs to mesoscale models such as free energies, stacking fault energies etc. Next, the correlation between the instability of B2 and the average valence electron count per atom could serve as a tool for alloy designers. For instance, the addition of elements in groups 7, and 8 could be a viable route to forming stable precipitates in refractory alloys with aluminum. The precise role of anti-site defects, and electronic structure in stabilizing B2-like orderings with aluminum compositions around 0.3 remains an open question.

3.2. Structural phase transformations

Longer ageing times of aluminum-containing refractory alloys invariably lead to the precipitation of more complex intermetallic phases. While complex phases are expected to nucleate at defects such as grain boundaries, recent research suggests that some of these phases may form within the ordered precipitates [38,74].

The high concentration of aluminum and zirconium in the ordered precipitate results in the formation of an intermetallic compound found along the Al–Zr binary. Fig. 13 shows the 0 K formation energies of 6 binary intermetallic compounds that have been reported to form in binary Al–Zr alloys. Though Al_3Zr_4 is the only stable complex intermetallic phase, all other phases have been reported to occur as either metastable phases or at elevated temperatures [64]. Sharma et al. [74] reported the formation of Al_4Zr_5, while Soni et al. [38] observed the

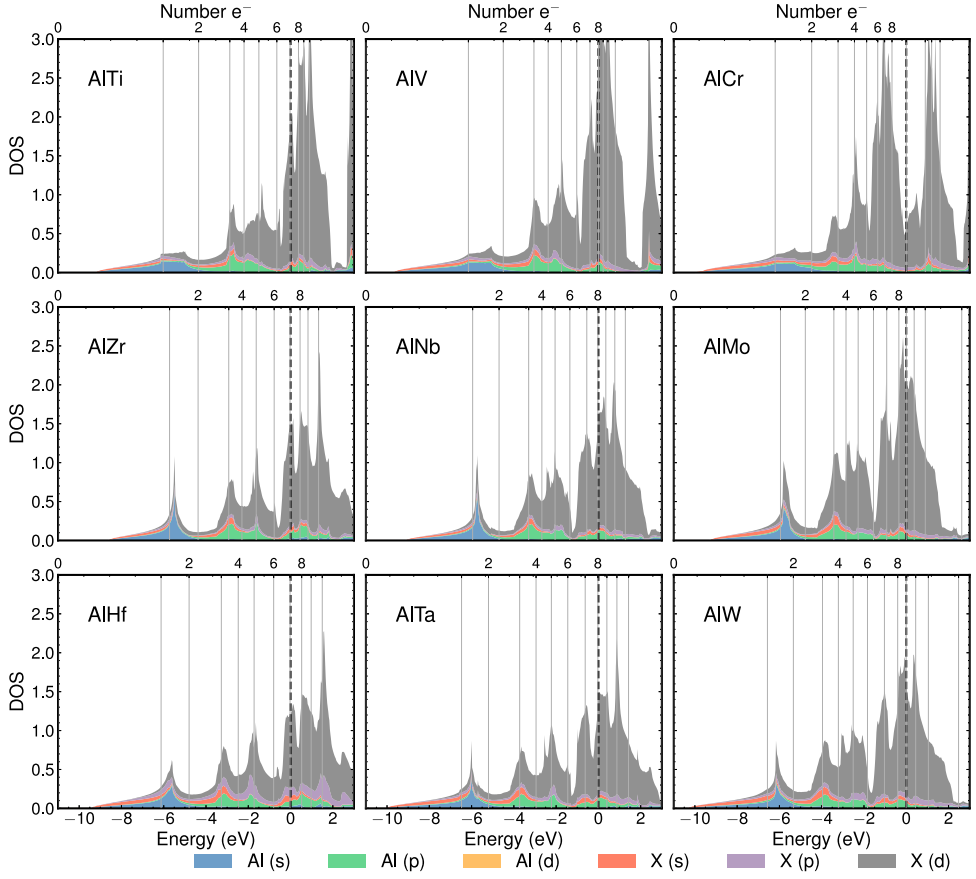

Fig. 11. Projected density of states of B2-AlX orderings, with X being an element of group 4, 5, or 6. The number of valence electrons per B2 cell is indicated on each plot.

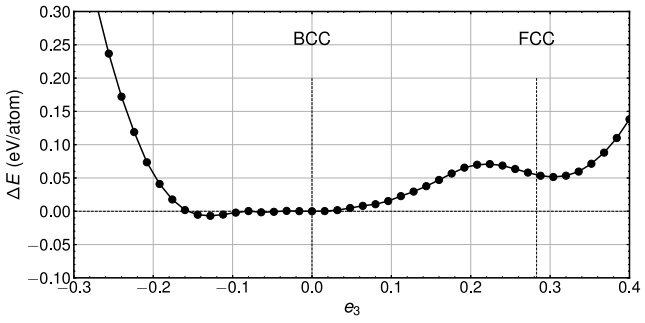

Fig. 12. Strain energy landscape for B2-AlRe along the Bain pathway.

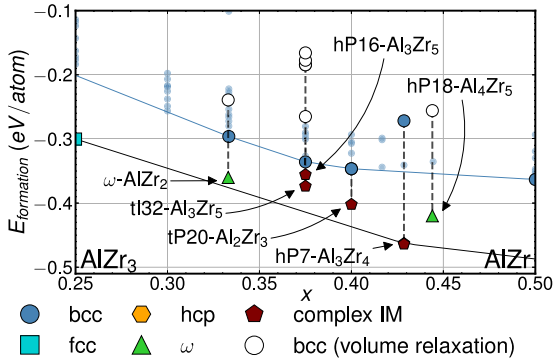

Fig. 13. Formation energies of orderings on the binary Al–Zr system. The equilibrium (black line) and metastable bcc (blue line) convex hulls are shown in the figure. Vertical dashed lines connect bcc orderings with the corresponding complex intermetallics that are experimentally observed. White circles correspond to orderings on bcc that relax to structures other than the complex intermetallics. Pathways between the unstable (white) structures and complex intermetallics were computed by only relaxing the volume of the endpoints. (For interpretation of the references to color in this figure legend, the reader is referred to the web version of this article.)

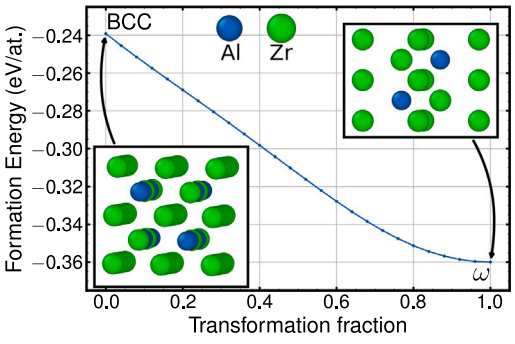

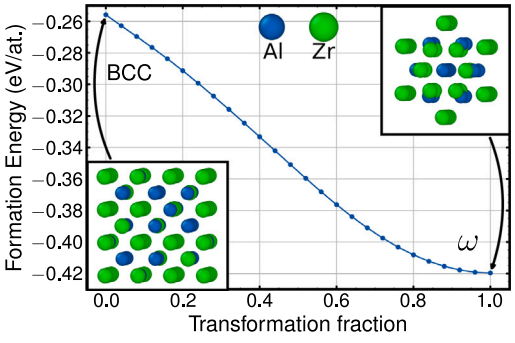

Fig. 14. Energy landscapes computed with DFT for a transformation pathway relating orderings on bcc to (a) $AlZr_2$ and (b) Al_4Zr_5.

precipitation of $AlZr_2$. Both phases are essentially orderings on the ω crystal structure. The crystal structures of hP16-Al_3Zr_5, tI32-Al_3Zr_5, tP20-Al_2Zr_3, and hP7-Al_3Zr_4 are more complicated. To analyze viable structural phase transformations, the structure mapping algorithm as implemented in the CASM software package [65] was employed to enumerate transformation pathways relating the complex intermetallic phases to orderings on the bcc crystal structure. Energy landscapes along the transition path were computed using DFT.

$AlZr_2$ and Al_4Zr_5 can be formed by transforming bcc to ω along the de Fontaine-Silcock pathway [75,76]. Our DFT calculations in Fig. 14, predict that orderings on bcc can undergo a barrierless homogeneous structural transformation to form ω. In contrast, as depicted in Fig. 15, hP16-Al_3Zr_5, tI32-Al_3Zr_5, tP20-Al_2Zr_3, and hP7-Al_3Zr_4 phases are all separated from orderings on bcc by a barrier. Interestingly, $AlZr_2$ can be derived from a bcc ordering where aluminum is segregated to a single B2 sublattice, while the formation of Al_4Zr_5 requires aluminum atoms to be dispersed over both sublattices of B2. B2-like orderings could also transform to form Al_3Zr_5, and Al_2Zr_3. However, our calculations predict a barrier separating the bcc phase from the more complex intermetallic phase. The ordering on the bcc phase that forms the Al_2Zr_3 structure is a ground state on the metastable bcc convex hull.

The transformation energy landscapes of Figs. 14 and 15 suggest a few potential nucleation pathways for more complex phases. The ordered B2-like precipitates could serve as potential nucleation sites for $AlZr_2$, Al_3Zr_5 and Al_2Zr_3. Local composition fluctuations within the ordered precipitate could nucleate the $AlZr_2$ phase that can grow and consume the precipitate over time. Similar ordering fluctuations within the disordered phase could serve as nucleation seeds for the formation of Al_4Zr_5 with the ω-like crystal structure. Due to the presence of barriers separating bcc from the complex intermetallic phases in Fig. 15, defects, such as grain boundaries, dislocations, stacking faults, etc. are likely to play a more significant role in the formation of the more complex intermetallic phases. Additional efforts are needed to rigorously quantify the homogeneous and heterogeneous nucleation mechanisms of these complex intermetallic phases.

4. Conclusion

Finite-temperature simulations with statistical mechanics techniques informed by first-principles electronic structure calculations were used to assess the thermodynamics of precipitation in a senary Al–Nb–Ta–Ti–V–Zr alloy. Precipitates observed in experiment are predicted to have B2-like order due to the strong segregation of aluminum to a single sublattice. Titanium and zirconium are predicted to partially disorder over both sublattices of B2 at elevated temperatures. Our models suggest that increasing aluminum and zirconium or vanadium and tantalum compositions may improve the solvus temperatures of the precipitate. However, increasing the aluminum and zirconium concentrations could also encourage the formation of more complex intermetallic phases. We have shown a clear correlation between the valence electron counts of B2-like orderings and their structural instabilities. Our results indicate that orderings such as B2, $L2_1$ and $D0_3$ are not representative of the true precipitate crystal structure due to their thermodynamic instability. Rather, the presence of more complex anti-site defects is necessary to stabilize ordered phases. Insights from this study suggest viable pathways to design better alloys for high-temperature applications through careful tuning of alloy chemistry.

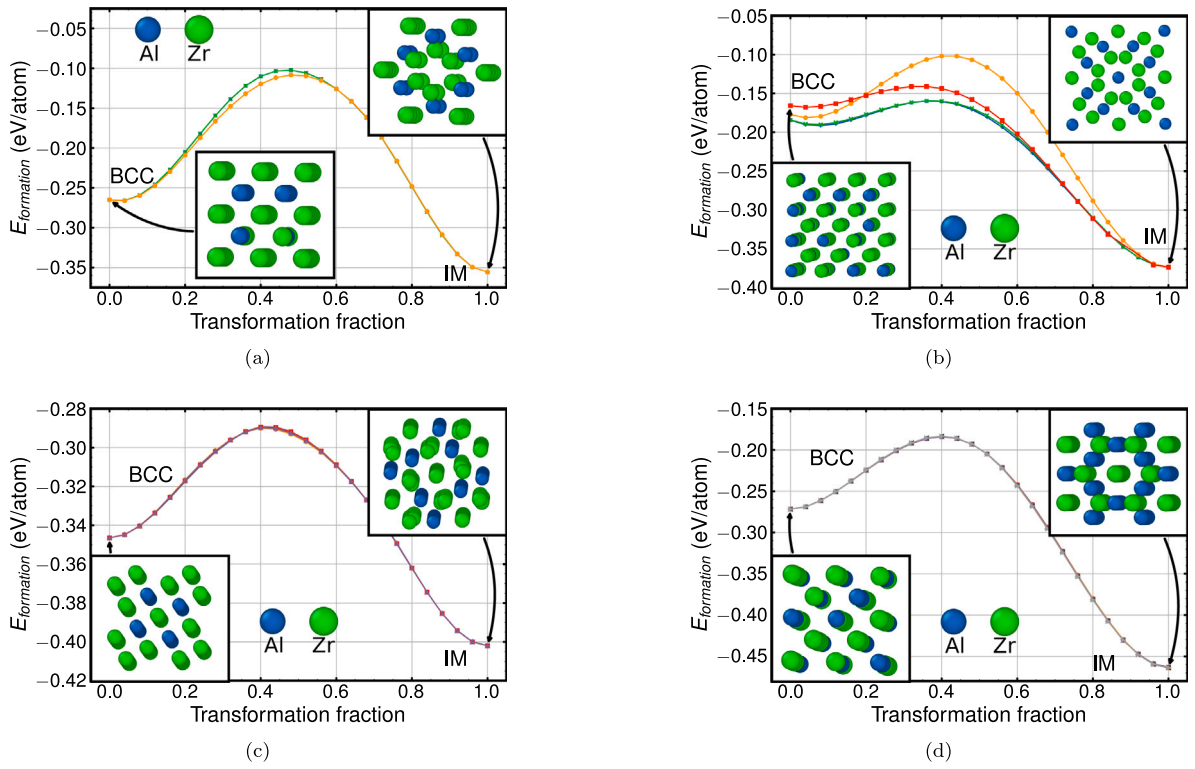

Fig. 15. Energy landscapes computed with DFT for transformation pathways relating orderings on bcc to intermetallic structures (a) hP16-Al_3Zr_5, (b) tI32-Al_3Zr_5, (c) tP20-Al_2Zr_3 and (d) hP7-Al_3Zr_4. The intermediate energies along the transformation pathways are obtained by only allowing for volume relaxation.

CRediT authorship contribution statement

Yann L. Müller: Formal analysis, Writing – original draft, Writing – review & editing. **Anirudh Raju Natarajan:** Conceptualization, Funding acquisition, Supervision, Writing – original draft, Writing – review & editing.

Declaration of competing interest

The authors declare that they have no known competing financial interests or personal relationships that could have appeared to influence the work reported in this paper.

Data availability

The data used in the present work is available through the MaterialsCloud (https://doi.org/10.24435/materialscloud:th-d5).

Acknowledgments

This research was supported by the NCCR MARVEL, Switzerland, a National Centre of Competence in Research, funded by the Swiss National Science Foundation, Switzerland (grant number 205602).

References

[1] S. Naka, T. Khan, Designing novel multiconstituent inter me tallies: Contribution of modern alloy theory in developing engineered materials, J. Phase Equilib. 18 (1997) 635.

[2] D. Miracle, Lightweighting and the future of aerospace metals, in: A.A. Gokhale, N.E. Prasad, B. Basu (Eds.), Light Weighting for Defense, Aerospace, and Transportation, in: Indian Institute of Metals Series, Springer, Singapore, 2019, pp. 27–38.

[3] D.B. Miracle, M.-H. Tsai, O.N. Senkov, V. Soni, R. Banerjee, Refractory high entropy superalloys (RSAs), Scr. Mater. 187 (2020) 445.

[4] G. Ouyang, P. Singh, R. Su, D.D. Johnson, M.J. Kramer, J.H. Perepezko, O.N. Senkov, D. Miracle, J. Cui, Design of refractory multi-principal-element alloys for high-temperature applications, npj Comput. Mater. 9 (2023) 1, number: 1 Publisher: Nature Publishing Group.

[5] L. Qi, D. Chrzan, Tuning ideal tensile strengths and intrinsic ductility of bcc refractory alloys, Phys. Rev. Lett. 112 (2014) 115503, publisher: American Physical Society.

[6] H. Zheng, L.T.W. Fey, X.-G. Li, Y.-J. Hu, L. Qi, C. Chen, S. Xu, I.J. Beyerlein, S.P. Ong, Multi-scale investigation of short-range order and dislocation glide in MoNbTi and TaNbTi multi-principal element alloys, npj Comput. Mater. 9 (2023) 1, number: 1 Publisher: Nature Publishing Group.

[7] D.B. Miracle, High entropy alloys as a bold step forward in alloy development, Nat. Commun. 10 (2019) 1805, number: 1 Publisher: Nature Publishing Group.

[8] O.N. Senkov, D.B. Miracle, S.I. Rao, Correlations to improve room temperature ductility of refractory complex concentrated alloys, Mater. Sci. Eng. A 820 (2021) 141512.

[9] C. Yang, L. Qi, Ab initio calculations of ideal strength and lattice instability in W-Ta and W-Re alloys, Phys. Rev. B 97 (2018) 014107, publisher: American Physical Society.

[10] A. Sundar, D.B. Ferron, Y.-J. Hu, L. Qi, Automated hierarchical screening of refractory multicomponent alloys with high intrinsic ductility and surface passivation potency, MRS Commun. 12 (2022) 1086.

[11] C. Tandoc, Y.-J. Hu, L. Qi, P.K. Liaw, Mining of lattice distortion, strength, and intrinsic ductility of refractory high entropy alloys, npj Comput. Mater. 9 (2023) 1, number: 1 Publisher: Nature Publishing Group.

[12] O.N. Senkov, C. Woodward, D.B. Miracle, Microstructure and properties of aluminum-containing refractory high-entropy alloys, JOM 66 (2014) 2030.

[13] O.N. Senkov, D.B. Miracle, K.J. Chaput, J.-P. Couzinie, Development and exploration of refractory high entropy alloys—A review, J. Mater. Res. 33 (2018) 3092.

[14] S. Laube, S. Schellert, A. Srinivasan Tirunilai, D. Schliephake, B. Gorr, H.-J. Christ, A. Kauffmann, M. Heilmaier, Microstructure tailoring of Al-containing compositionally complex alloys by controlling the sequence of precipitation and ordering, Acta Mater. 218 (2021) 117217.

[15] C. Wolverton, Crystal structure and stability of complex precipitate phases in Al–Cu–Mg–(Si) and Al–Zn–Mg alloys, Acta Mater. 49 (2001) 3129.

[16] A.R. Natarajan, E.L.S. Solomon, B. Puchala, E.A. Marquis, A. Van der Ven, On the early stages of precipitation in dilute Mg–Nd alloys, Acta Mater. 108 (2016) 367.

[17] R.W. Balluffi, S.M. Allen, W.C. Carter, Kinetics of Materials, John Wiley & Sons, 2005.

[18] D.A. Porter, K.E. Easterling, Phase Transformations in Metals and Alloys (Revised Reprint), CRC press, 2009.

[19] P. Caron, T. Khan, Evolution of Ni-based superalloys for single crystal gas turbine blade applications, Aerosp. Sci. Technol. 3 (1999) 513.

[20] M. Dodaran, A.H. Ettefagh, S.M. Guo, M.M. Khonsari, W.J. Meng, N. Shamsaei, S. Shao, Effect of alloying elements on the γ' antiphase boundary energy in Ni-base superalloys, Intermetallics 117 (2020) 106670.

[21] E. Chen, A. Tamm, T. Wang, M.E. Epler, M. Asta, T. Frolov, Modeling antiphase boundary energies of Ni3Al-based alloys using automated density functional theory and machine learning, npj Comput. Mater. 8 (2022) 1.

[22] R.C. Reed, The Superalloys: Fundamentals and Applications, Cambridge University Press, 2008.

[23] A.R. Natarajan, P. Dolin, A. Van der Ven, Crystallography, thermodynamics and phase transitions in refractory binary alloys, Acta Mater. 200 (2020) 171.

[24] D.B. Miracle, High-entropy alloys: A current evaluation of founding ideas and core effects and exploring nonlinear alloys, JOM 69 (2017) 2130.

[25] O.N. Senkov, C.F. Woodward, Microstructure and properties of a refractory NbCrMo0.5Ta0.5TiZr alloy, Mater. Sci. Eng. A 529 (2011) 311.

[26] O.N. Senkov, J.M. Scott, S.V. Senkova, D.B. Miracle, C.F. Woodward, Microstructure and room temperature properties of a high-entropy TaNbHfZrTi alloy, J. Alloys Compd. 509 (2011) 6043.

[27] O.N. Senkov, G.B. Wilks, J.M. Scott, D.B. Miracle, Mechanical properties of Nb25Mo25Ta25W25 and V20Nb20Mo20Ta20W20 refractory high entropy alloys, Intermetallics 19 (2011) 698.

[28] O.N. Senkov, S.V. Senkova, C. Woodward, D.B. Miracle, Low-density, refractory multi-principal element alloys of the Cr–Nb–Ti–V–Zr system: Microstructure and phase analysis, Acta Mater. 61 (2013) 1545.

[29] C. Wolverton, V. Ozoliņš, First-principles aluminum database: Energetics of binary Al alloys and compounds, Phys. Rev. B 73 (2006) 144104, publisher: American Physical Society.

[30] E.A. Anber, N.C. Smith, P.K. Liaw, C.M. Wolverton, M.L. Taheri, Role of Al additions in secondary phase formation in CoCrFeNi high entropy alloys, APL Mater. 10 (2022) 101108.

[31] N.D. Stepanov, D.G. Shaysultanov, G.A. Salishchev, M.A. Tikhonovsky, Structure and mechanical properties of a light-weight AlNbTiV high entropy alloy, Mater. Lett. 142 (2015) 153.

[32] N.Y. Yurchenko, N.D. Stepanov, D.G. Shaysultanov, M.A. Tikhonovsky, G.A. Salishchev, Effect of Al content on structure and mechanical properties of the AlxCrNbTiVZr (x=0; 0.25; 0.5; 1) high-entropy alloys, Mater. Charact. 121 (2016) 125.

[33] N.Y. Yurchenko, N.D. Stepanov, S.V. Zherebtsov, M.A. Tikhonovsky, G.A. Salishchev, Structure and mechanical properties of B2 ordered refractory AlNbTiVZrx (x=0–1.5) high-entropy alloys, Mater. Sci. Eng. A 704 (2017) 82.

[34] Y. Qiu, Y.J. Hu, A. Taylor, M.J. Styles, R.K.W. Marceau, A.V. Ceguerra, M.A. Gibson, Z.K. Liu, H.L. Fraser, N. Birbilis, A lightweight single-phase AlTiVCr compositionally complex alloy, Acta Mater. 123 (2017) 115.

[35] N.Y. Yurchenko, N.D. Stepanov, A.O. Gridneva, M.V. Mishunin, G.A. Salishchev, S.V. Zherebtsov, Effect of Cr and Zr on phase stability of refractory Al-Cr-Nb-Ti-V-Zr high-entropy alloys, J. Alloys Compd. 757 (2018) 403.

[36] F.G. Coury, T. Butler, K. Chaput, A. Saville, J. Copley, J. Foltz, P. Mason, K. Clarke, M. Kaufman, A. Clarke, Phase equilibria, mechanical properties and design of quaternary refractory high entropy alloys, Mater. Des. 155 (2018) 244.

[37] H. Chen, A. Kauffmann, S. Seils, T. Boll, C.H. Liebscher, I. Harding, K.S. Kumar, D.V. Szabó, S. Schlabach, S. Kauffmann-Weiss, F. Müller, B. Gorr, H.J. Christ, M. Heilmaier, Crystallographic ordering in a series of Al-containing refractory high entropy alloys Ta–Nb–Mo–Cr–Ti–Al, Acta Mater. 176 (2019) 123.

[38] V. Soni, O.N. Senkov, J.P. Couzinie, Y. Zheng, B. Gwalani, R. Banerjee, Phase stability and microstructure evolution in a ductile refractory high entropy alloy Al10Nb15Ta5Ti30Zr40, Materialia 9 (2020) 100569.

[39] V. Soni, B. Gwalani, T. Alam, S. Dasari, Y. Zheng, O.N. Senkov, D. Miracle, R. Banerjee, Phase inversion in a two-phase, BCC+B2, refractory high entropy alloy, Acta Mater. 185 (2020) 89.

[40] S. Laube, H. Chen, A. Kauffmann, S. Schellert, F. Müller, B. Gorr, J. Müller, B. Butz, H.-J. Christ, M. Heilmaier, Controlling crystallographic ordering in Mo–Cr–Ti–Al high entropy alloys to enhance ductility, J. Alloys Compd. 823 (2020) 153805.

[41] D. Qiao, H. Liang, S. Wu, J. He, Z. Cao, Y. Lu, T. Li, The mechanical and oxidation properties of novel B2-ordered Ti2ZrHf0.5VNb0.5Alx refractory high-entropy alloys, Mater. Charact. 178 (2021) 111287.

[42] S. Laube, A. Kauffmann, S. Schellert, S. Seils, A.S. Tirunilai, C. Greiner, Y.M. Eggeler, B. Gorr, H.-J. Christ, M. Heilmaier, Formation and thermal stability of two-phase microstructures in Al-containing refractory compositionally complex alloys, Sci. Technol. Adv. Mater. 23 (2022) 692, 36337083.

[43] C. Frey, R. Silverstein, T.M. Pollock, A high stability B2-containing refractory multi-principal element alloy, Acta Mater. 229 (2022) 117767.

[44] J.E. Saal, S. Kirklin, M. Aykol, B. Meredig, C. Wolverton, Materials design and discovery with high-throughput density functional theory: The open quantum materials database (OQMD), JOM 65 (2013) 1501.

[45] S. Kirklin, J.E. Saal, B. Meredig, A. Thompson, J.W. Doak, M. Aykol, S. Rühl, C. Wolverton, The open quantum materials database (OQMD): assessing the accuracy of DFT formation energies, npj Comput. Mater. 1 (2015) 1, number: 1 Publisher: Nature Publishing Group.

[46] A. Jain, S.P. Ong, G. Hautier, W. Chen, W.D. Richards, S. Dacek, S. Cholia, D. Gunter, D. Skinner, G. Ceder, K.A. Persson, Commentary: The materials project: A materials genome approach to accelerating materials innovation, APL Mater. 1 (2013) 011002.

[47] S. Curtarolo, W. Setyawan, G.L.W. Hart, M. Jahnatek, R.V. Chepulskii, R.H. Taylor, S. Wang, J. Xue, K. Yang, O. Levy, M.J. Mehl, H.T. Stokes, D.O. Demchenko, D. Morgan, AFLOW: An automatic framework for high-throughput materials discovery, Comput. Mater. Sci. 58 (2012) 218.

[48] J.-P. Couzinié, M. Heczko, V. Mazánová, O.N. Senkov, M. Ghazisaeidi, R. Banerjee, M.J. Mills, High-temperature deformation mechanisms in a BCC+B2 refractory complex concentrated alloy, Acta Mater. 233 (2022) 117995.

[49] J.M. Sanchez, F. Ducastelle, D. Gratias, Generalized cluster description of multicomponent systems, Phys. A 128 (1984) 334.

[50] D. De Fontaine, Cluster approach to order–disorder transformations in alloys, in: Solid state physics, vol. 47, Elsevier, 1994, pp. 33–176.

[51] B. Puchala, J.C. Thomas, A.R. Natarajan, J.G. Goiri, S.S. Behara, J.L. Kaufman, A. Van der Ven, CASM — A software package for first-principles based study of multicomponent crystalline solids, Comput. Mater. Sci. 217 (2023) 111897.

[52] A. Van der Ven, J. Thomas, B. Puchala, A. Natarajan, First-principles statistical mechanics of multicomponent crystals, Annu. Rev. Mater. Res. 48 (2018) 27, http://dx.doi.org/10.1146/annurev-matsci-070317-124443, _eprint:.

[53] B. Puchala, A. Van der Ven, Thermodynamics of the Zr-O system from first-principles calculations, Phys. Rev. B 88 (2013) 094108, publisher: American Physical Society.

[54] J.C. Thomas, A. Van der Ven, Finite-temperature properties of strongly anharmonic and mechanically unstable crystal phases from first principles, Phys. Rev. B 88 (2013) 214111.

[55] P.E. Blöchl, Projector augmented-wave method, Phys. Rev. B 50 (1994) 17953.

[56] G. Kresse, D. Joubert, From ultrasoft pseudopotentials to the projector augmented-wave method, Phys. Rev. B 59 (1999) 1758.

[57] R. Tibshirani, Regression shrinkage and selection via the lasso, J. R. Stat. Soc. Ser. B Stat. Methodol. 58 (1996) 267.

[58] F. Pedregosa, G. Varoquaux, A. Gramfort, V. Michel, B. Thirion, O. Grisel, M. Blondel, P. Prettenhofer, R. Weiss, V. Dubourg, J. Vanderplas, A. Passos, D. Cournapeau, M. Brucher, M. Perrot, E. Duchesnay, Scikit-learn: Machine learning in python, J. Mach. Learn. Res. 12 (2011) 2825.

[59] A. Zunger, S.-H. Wei, L. Ferreira, J.E. Bernard, Special quasirandom structures, Phys. Rev. Lett. 65 (1990) 353.

[60] H. von Helmholtz, Die thermodynamik chemischer vorgange, Ber. KGL. Preuss. Akad. Wiss. Berlin 1 (1882) 22.

[61] A.R. Natarajan, J.C. Thomas, B. Puchala, A. Van der Ven, Symmetry-adapted order parameters and free energies for solids undergoing order–disorder phase transitions, Phys. Rev. B 96 (2017) 134204.

[62] J. Murray, A. Peruzzi, J.P. Abriata, The Al-Zr (aluminum-zirconium) system, J. Phase Equilib. 13 (1992) 277.

[63] F. Yang, F.H. Xiao, S.G. Liu, S.S. Dong, L.H. Huang, Q. Chen, G.M. Cai, H.S. Liu, Z.P. Jin, Isothermal section of Al–Ti–Zr ternary system at 1273K, J. Alloys Compd. 585 (2014) 325.

[64] Z. Kahrobaee, M. Palm, Critical assessment of the Al-Ti-Zr system, J. Phase Equilibria Diffusion 41 (2020) 687.

[65] J.C. Thomas, A.R. Natarajan, A. Van der Ven, Comparing crystal structures with symmetry and geometry, npj Comput. Mater. 7 (2021) 1, number: 1 Publisher: Nature Publishing Group.

[66] M. Ångqvist, J.M. Rahm, L. Gharaee, P. Erhart, Structurally driven asymmetric miscibility in the phase diagram of w-ti, Phys. Rev. Mater. 3 (2019) 073605.

[67] N.H. Gunda, A. Van der Ven, Understanding the interactions between interstitial and substitutional solutes in refractory alloys: The case of Ti-Al-O, Acta Mater. 191 (2020) 149.

[68] C. Reynolds, T.M. Pollock, A. Van der Ven, Solute-solute interactions in dilute nb-xo alloys from first principles, Acta Mater. 266 (2024) 119621.

[69] A. Raju Natarajan, A. Van der Ven, Toward an understanding of deformation mechanisms in metallic lithium and sodium from first-principles, Chem. Mater. 31 (2019) 8222, publisher: American Chemical Society.

[70] D. Pettifor, Theory of the crystal structures of transition metals, J. Phys. C: Solid State Phys. 3 (1970) 367.

[71] D. Pettifor, A physicist's view of the energetics of transition metals, CALPHAD 1 (1977) 305.

[72] H.L. Skriver, Crystal structure from one-electron theory, Phys. Rev. B 31 (1985) 1909.

[73] B. Feng, M. Widom, Band structure theory of the bcc to hcp burgers distortion, Phys. Rev. B 98 (2018) 174108.

[74] A. Sharma, S. Dasari, V. Soni, Z. Kloenne, J.-P. Couzinié, O.N. Senkov, D.B. Miracle, S.G. Srinivasan, H. Fraser, R. Banerjee, B2 to ordered omega transformation during isothermal annealing of refractory high entropy alloys: implications for high temperature phase stability, J. Alloys Compd. 953 (2023) 170065.

[75] D. De Fontaine, Mechanical instabilities in the b.c.c. lattice and the beta to omega phase transformation, Acta Metall. 18 (1970) 275.

[76] J.M. Silcock, An X-ray examination of the to phase in TiV, TiMo and ticr alloys, Acta Metall. 6 (1958) 481.